Exploring the Planar Circular Restricted Three-body Problem with Prolate Primaries

Euaggelos E. Zotos[1],[†]

Abstract We numerically investigate the convergence properties of the circular restricted three-body problem with prolate primaries, by using the Newton-Raphson iterative scheme. In particular, we examine how the oblateness coefficient A influences several aspects of the method, such as its speed and efficiency. Color-coded diagrams are used for revealing the basins of convergence on the configuration space. Additionally, we compute the degree of fractality of the convergence basins on the physical plane, as a function of the oblateness coefficient, by using different computational tools, such as the uncertainty dimension and the (boundary) basin entropy.

Keywords Restricted three-body problem, Oblateness parameter, Basins of convergence.

MSC(2010) 37N05, 37N30, 37N05.

1. Introduction

According to [1] in the original version of the restricted three-body problem (RTBP) the shape of the two primary bodies is assumed to be spherically symmetric. However, for obtaining a more realistic and complete representation regarding the nature of the motion of a body acting as a test particle, especially in the Solar System, a plethora of modifications have been proposed, over the years. All these modifications aim to include in the effective potential the influence of additional dynamical parameters, such as the shape or the radiation of the primary bodies.

It is well known that in our Solar System many celestial bodies (e.g., Saturn and Jupiter, as well many minor natural satellites) have a spheroidal shape [2]. For incorporating the particular shape of the primaries into the equations explaining the motion of the test body (e.g., comet, asteroid, or spacecraft) the oblateness parameter has been introduced and used initially in [3]. From then, a large amount of research work has been devoted on the study of the influence of the oblateness (see e.g., [4–16]).

As we know, in the original version of the RTBP there exist five equilibrium or Lagrange points. Unfortunately, there is the misbelief that the same number of points of equilibrium also exists in the case where the primary bodies are spheroidals, thus taking into account the oblateness coefficient. This however is correct only in the case of oblate primaries, where five equilibrium points are present for every positive value of the oblateness coefficient [17]. In the case of prolate primaries,

———————————————

[†]the corresponding author.

  Email address: evzotos@physics.auth.gr(E. E. Zotos)

[1]Department of Physics, School of Science, Aristotle University of Thessaloniki, GR-541 24, Thessaloniki, Greece

that is when the parameter of the oblateness has negative values, the number of the equilibrium points is not constant, but a function of the oblateness. In the present paper we are going to present in detail the equilibrium points along with their linear stability, in the case of prolate primaries.

Knowing the coordinates of the points of equilibrium of a system is an issue of high importance. However, this is not possible for many complicated dynamical systems for which there are no analytical equations for the positions of the equilibrium points. This automatically means that only by using numerical methods we can obtain the locations of the libration points. As we know, in all numerical methods the initial conditions are very important. This is true because for some starting points the numerical methods may converge relatively fast to a root, while for other initial points they may require a considerable amount of iterations. Usually, points with fast convergence belong to the so-called basins of convergence (BOC), while points with slow convergence are situated in the vicinity of the fractal basin boundaries. Therefore, it is very important to know the location of the BOC for a dynamical system, because then we automatically are aware of the optimal initial conditions for the numerical methods. Here, we would like to point out that the BOC of a dynamical system strongly depend on the chosen numerical method. In other words, different numerical methods yield to completely different BOC, for the same dynamical system.

In Section 2 we provide the mathematical description of the dynamical model, while in the following section 3 we present the parametric evolution of the coordinates and the stability of the points of equilibrium. Section 4 we illustrate the geometry along with the basic properties of the Newton-Raphson BOC, while the Section 5 is devoted on determining the influence of the oblateness on the properties of the system of three bodies. In the final Section 6 we provide the discussion of our work.

2. Mathematical description of the dynamical system

The restricted three-body system (RTBP) contains two massive bodies P_1 and P_2 (known as the primaries), while the third body is assumed to act as a test particle [1]. This means that the mass m of the test particle is significantly smaller, comparing with masses m_1 and m_2 of the two primary bodies. The two main bodies rotate in circular orbits around their gravitational center (which is common), while the motion of the third body does have any dynamical impact on the motion of the primaries, due to its insignificant mass.

For convenience, we use a units system where the distance R, between the centers of the two main bodies, and the constant of gravity G are both equal to unity. Using the mass parameter $\mu = m_2/(m_1 + m_2) \leq 1/2$ we can express the dimensionless masses of the two main bodies as $m_1 = 1 - \mu$ and $m_2 = \mu$. Both centers of the primaries are located at $(x_1, 0, 0)$ and $(x_2, 0, 0)$ (on the x-axis), where of course $x_1 = -\mu$ and $x_2 = 1 - \mu$. In our analysis we use a rotating barycentric frame of reference $Oxyz$, where the Ox axis is the line containing the centers of the primaries, while the origin $(0, 0)$ of the system of coordinates coincides with the mass center of the primaries. Fig. 1 shows a schematic of the configuration of the system of bodies.
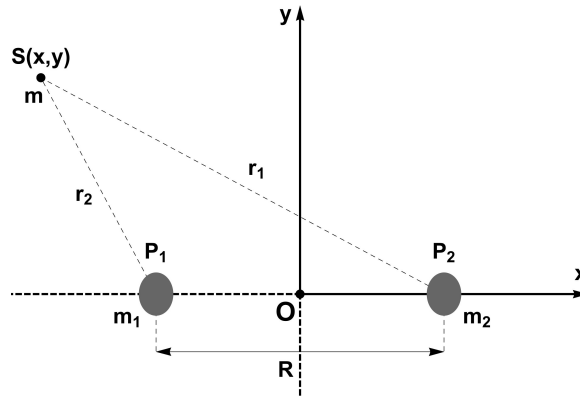
Figure 1. The planar configuration of the RTBP system, with prolate primaries.

In the case of spheroidal primaries, with oblateness coefficients A_i, $i = 1, 2$, the effective potential of the planar system (with $z = 0$) is, according to [3],

$$\Omega(x, y) = \sum_{n=1}^{2} \left(\frac{m_i}{r_i} \left(1 + \frac{A_i}{2r_i^2} \right) \right) + \frac{n^2}{2} \left(x^2 + y^2 \right), \tag{2.1}$$

where

$$r_1 = \sqrt{(x - x_1)^2 + y^2},$$
$$r_2 = \sqrt{(x - x_2)^2 + y^2}, \tag{2.2}$$

are the relations of the distances between the test particle and the centers of the two primaries. The mean motion (n) is given by

$$n = \sqrt{1 + \frac{3}{2} (A_1 + A_2)}. \tag{2.3}$$

In the present study we will focus on the case with prolate spheroidal primaries $(A < 0)$, where the value of the oblateness lie in the interval $[-1, 0]$. In order to have only one free parameter we consider the Copenhagen problem with primaries of equal masses $\mu = 1/2$. In addition, both prolate bodies will have the same value of the oblateness, that is when $A_1 = A_2 = A$. This fact (the only one variable parameter) allow us to investigate in detail the effect of the oblateness A on several properties of the Hamiltonian system.

The planar motion of the third body is governed by the following set of equations

$$\ddot{x} - 2n\dot{y} = \frac{\partial \Omega}{\partial x}, \quad \ddot{y} + 2n\dot{x} = \frac{\partial \Omega}{\partial y}, \tag{2.4}$$

where as usual the time derivatives are denoted using dots.

The Hamiltonian of the dynamical system reads

$$J(x, y, \dot{x}, \dot{y}) = 2\Omega(x, y) - \left(\dot{x}^2 + \dot{y}^2 \right) = C. \tag{2.5}$$

The total orbital energy E is related with the Jacobi constat through the equation $C = -2E$.
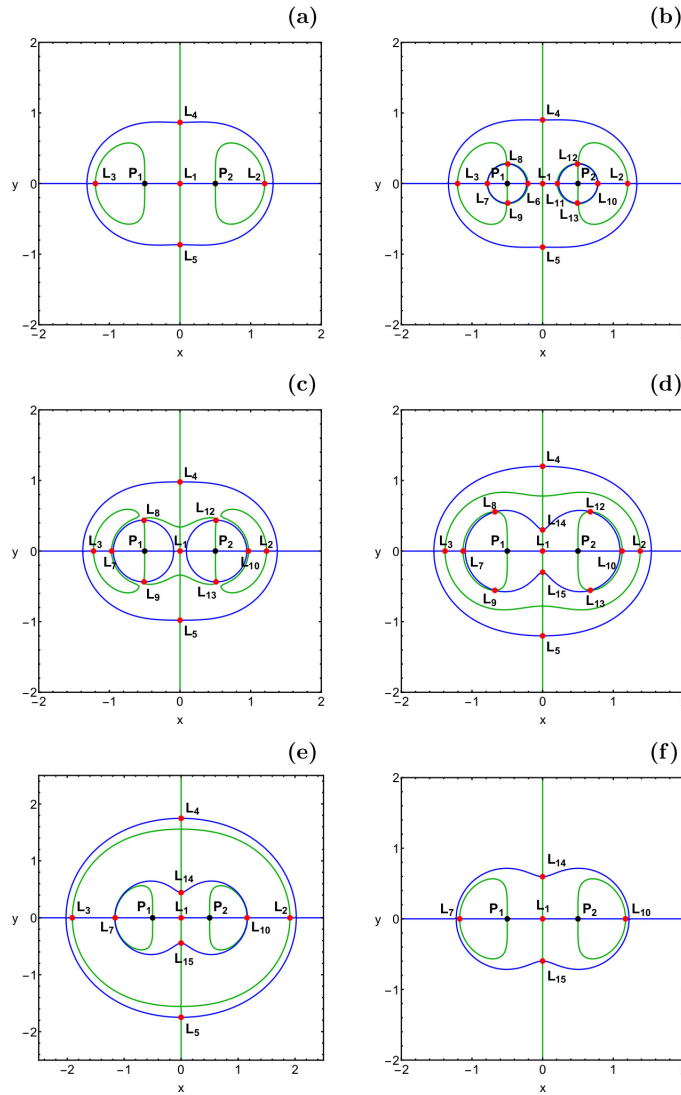
Figure 2. The intersections of the contours of the equations $\Omega_x = 0$ (green) and $\Omega_y = 0$ (blue) pinpoint the locations (red dots) of the equilibrium points (L_i, $i = 1, 15$). (a): $A = 0$; (b): $A = -0.05$; (c): $A = -0.12$; (d) $A = -0.21$; (e): $A = -0.285$; (f): $A = -0.5$. The centers of the two primaries (P_i, $i = 1, 2$) are indicated using black dots. (Color figure online).

3. Location and stability of equilibrium points

In a Hamiltonian system an equilibrium point exists if and only if (necessary and sufficient conditions)

$$\dot{x} = \dot{y} = \ddot{x} = \ddot{y} = 0. \tag{3.1}$$

On this basis, for obtaining the coordinates (x_0, y_0) of the coplanar points of equilibrium of the RTBP, with prolate primaries, all we have to to do is to solve the
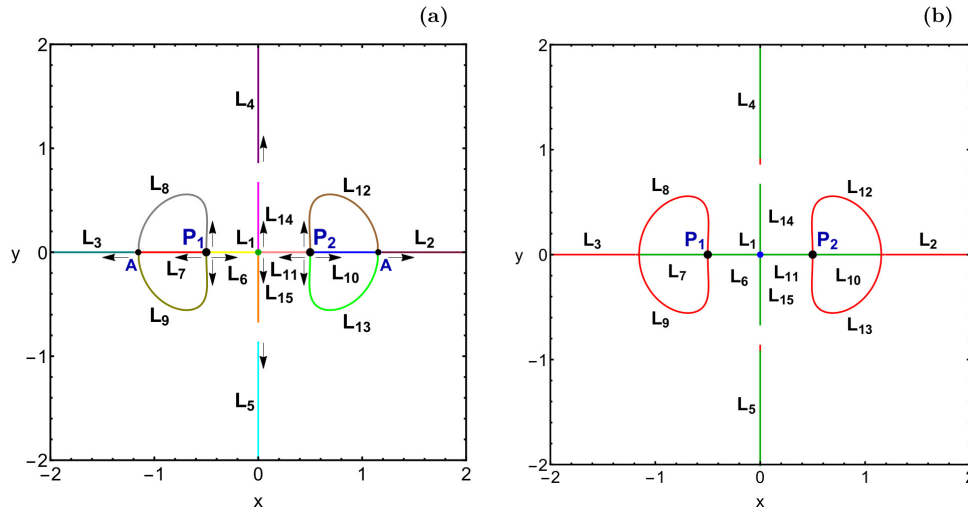
Figure 3. The evolution on the configuration space (x, y) of the (a-left): coordinates and (b-right): linear stability (green) or instability (red) of the points of equilibrium in the RTBP with prolate primaries, when $A \in [-1, 0)$. The small arrows indicate how the libration points move, as the value of A reduces. The two centers of the primaries are pinpointed by big black dots, while points A (small black dots) correspond to $A = A_3$. (Color figure online).

system

$$
\begin{cases}
\Omega_x(x, y) = 0 \\
\Omega_y(x, y) = 0
\end{cases} \tag{3.2}
$$

At this point, it should be emphasized that the above system of equations does not have analytical solutions in closed form, which automatically means that the coordinates of the libration point of the system can be derived only by using numerical methods.

Our numerical analysis reveals that the oblateness parameter of the primaries has a major impact on the total number of points of equilibrium. In particular:

- When $A \in [-0.08717948, 0)$ the dynamical system has 13 coplanar points of equilibrium (see part (b) of Fig. 2).

- When $A \in [-7/45, -0.08717949]$ the dynamical system has 11 points of equilibrium (see part (c) of Fig. 2).

- When $A \in [-0.27066806, -7/45)$ the dynamical system has 13 points of equilibrium (see part (d) of Fig. 2).

- When $A \in [-1/3, -0.27066807]$ the dynamical system has 9 points of equilibrium (see part (e) of Fig. 2).

- When $A < -1/3$ the dynamical system has 9 points of equilibrium (see part (f) of Fig. 2).

The values $A_1 = -0.08717948$, $A_2 = -7/45$, $A_3 = -0.27066806$, and $A_4 = -1/3$ are critical values of the oblateness parameter, which divide the interval $[-1, 0]$ into five regions, with different total number of equilibrium points.

The positions of the coordinates of the libration points on the configuration space (x, y) correspond to the intersections of the equations $\Omega_x = 0$ and $\Omega_y = 0$.

In Fig. 2 we present the locations of the equilibrium points, for six values of the oblateness A, including, as a reference, the classical case with $A = 0$. It should be noted, that when $A < -1/3$ (see penal (f) of Fig. 2) the structure of the contours is very similar to that of the classical RTBP (see panel (a) of Fig. 2).

In panel (a) of Fig. 3 we illustrate the evolution on the configuration space (x, y) of the points of equilibrium, as the value of the oblateness starts from 0 and continues up to $A = -1$. When $A = 0$ we have the well known five equilibrium points of the classical RTBP. When $A < 0$ two sets of four additional libration points emerge from the centers of the primaries. Each set is composed of two collinear points and two points with $y \neq 0$. As the value of A tends to the first critical value A_1 the collinear points L_6 and L_{11} tend to the origin and when $A = A_1$ both of them collide with the central equilibrium point L_1 and they disappear. At the same time, the libration points L_2, L_3, L_4 and L_5 move away from the origin. Just below the seconds critical value A_2 two new equilibrium points, L_{14} and L_{15}, emerge from the origin and they start to move on the vertical y axis. With further decreasing value of A the four libration points with $y = 0$ start to converge to the horizontal axis. When $A = A_3$, L_8 and L_9 collide with L_7, while L_{12} and L_{13} collide with L_{10} and all four equilibrium points L_8, L_9, L_{12}, and L_{13} are annihilated. As we proceed to even lower values of A the equilibrium points L_2, L_3, L_4 and L_5 start to quickly diverge from the rest of the libration points. Our computations indicate that these four points tend asymptotically to $\pm\infty$ when $A \to A_4 = -1/3$. For $A < A_4$ only five equilibrium points survive, while their positions display very small changes for even lower values of the oblateness parameter. It should be noted, that the parameter A has no influence on the centers of the two primaries, which remain unperturbed.

There is no doubt that apart from the positions of the points of equilibrium one should also be aware of their linear stability. For obtaining the linear stability of the points of equilibrium we computed the corresponding four roots of the characteristic equation, by following the numerical method explained in detail in [18]. When $A \in [-1, 0)$ we found that:

- The equilibrium point L_1 is linearly stable only when $A \in (A_2, A_1)$ and unstable in all other cases.

- The equilibrium points L_2, L_3, L_8, L_9, L_{12}, and L_{13} are always linearly unstable.

- The equilibrium points L_4 and L_5 are linearly unstable when $A \in (-0.07249094, 0)$ and stable in all other cases.

- The equilibrium points L_6, L_{11}, L_{14}, and L_{15} are always linearly stable.

- The equilibrium points L_7 and L_{10} are linearly stable when $A \in (A_3, 0)$ and unstable in all other cases.

4. The Newton-Raphson basins of attraction

In this section, we will present the shapes and features of the BOC on the configuration space (x, y), for several characteristic values of the oblateness A. For numerically solving the system of equations (3.2) we use the following Newton-Raphson (NR) iterative scheme

$$x_{n+1} = x_n - \left(\frac{\Omega_x \Omega_{yy} - \Omega_y \Omega_{xy}}{\Omega_{yy} \Omega_{xx} - \Omega_{xy}^2} \right)_{(x_n, y_n)},$$

$$y_{n+1} = y_n + \left(\frac{\Omega_x \Omega_{yx} - \Omega_y \Omega_{xx}}{\Omega_{yy} \Omega_{xx} - \Omega_{xy}^2} \right)_{(x_n, y_n)}, \tag{4.1}$$

while all the details of how the numerical procedure of obtaining the BOC works are described in Section 4 of [18].

In the following for visualizing the BOC on the configuration space (x, y) we will deploy two-dimensional diagrams with a color code. In these plots, each point (initial condition) receives a color which corresponds to the respective numerical attractor (point of equilibrium), thus following the pioneer graphical approach introduced and used in [19, 20].

4.1. Case I: 13 equilibrium points

In the first column of Fig. 4 we depict the BOC for three values of the oblateness in the first interval $[A_1, 0)$, where 13 equilibrium points are present. The diagrams on the second column of the same figure shows how the number of the required iterations is distributed on the configuration space (x, y), while the last column contains the probability histograms, corresponding to the required number of iterations.

With decreasing value of the oblateness we see that the area of the BOC grows rapidly and especially the regions corresponding to the equilibrium points L_6 and L_{11}, the shape of which resembles butterfly wings. When $A = -0.08717$, that is a level close to the first critical level of A, an interesting behaviour is observed at the last column of Fig. 4. More specifically, one can observe that inside the butterfly wings shaped BOC there exist a chaotic mixture of converging and non-converging initial conditions. This chaotic (or noisy) mixture is more evident in panel (h) of Fig. 4 where we see that almost the entire configuration space (x, y) is covered by starting points for which the numerical method requires arbitrary (chaotic) high or low number of iterations. Moreover, in panel (i) it is observed that the range of required number of iterations has been increased, with respect to the previous two cases (shown in the first two rows). We suspect that the appearance of non-converging initial conditions is due to the fact that we approach the first critical level of A, where the dynamics of the system change.

4.2. Case II: 11 equilibrium points

Fig. 5 shows the numerical results of three cases in the second interval (A_2, A_1), when the dynamical system has 11 equilibrium points. The first row of Fig. 5 corresponds to $A = -0.08718$, that is a value of oblateness just below the first critical level A_1. Once more we observe a similar behavior to that discussed earlier, where non-converging initial conditions appear. In this case however, their present is more prominent. Panels (b) and (c) of the Fig. 5 reveal that the configuration space (x, y) is divided into two main areas: (i) the central region, where the BOC lie and the required iterations are low ($N < 15$) and (ii) the outer chaotic region, where the initial conditions cover entirely randomly (or noisy) all the available range of allowed iterations $N \in [0, 500]$. Again, the reason of this strange behavior should be related with the fact that the specific value of the oblateness is very close to one of the critical levels.

As the value of A decreases, thus tending to the second critical level A_2, it is seen in the second and third row of Fig. 5 that the overall area of the BOC grows significantly. More specifically, one can observe the existence of thin tentacles which
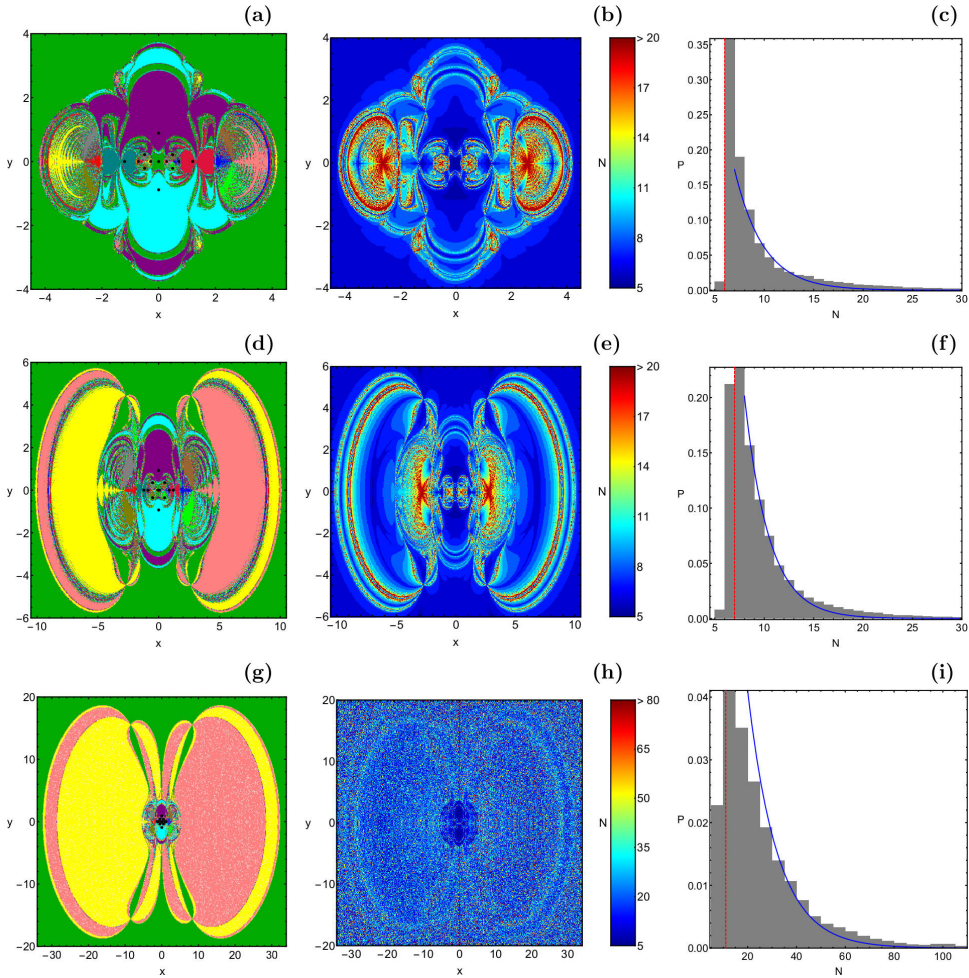
Figure 4. (First column): Color-coded plots showing the NR BOC on the configuration space (x, y), when 13 equilibrium points exist. The colors denoting the 13 numerical attractors (libration points) are as follows: L_1 (Darker green); L_2 (Crimson); L_3 (Teal); L_4 (Purple); L_5 (Cyan); L_6 (Yellow); L_7 (Red); L_8 (Gray); L_9 (Olive); L_{10} (Blue); L_{11} (Pink); L_{12} (Brown); L_{13} (Green); non-converging points (white). (Second column): Distributions of the corresponding required numbers of iterations. (Third column): Histograms with the corresponding probability distributions. (First row): $A = -0.03$; (Second row): $A = -0.08$; (Third row): $A = -0.0871$. (Color figure online).

emerge from the central region and extend to large distances from the center. Note that close to the boundaries of these tentacles the required number of iterations is considerable higher, with respect to that corresponding to the central basins.

4.3. Case III: 13 equilibrium points

The NR BOC in the third interval (A_3, A_2), when 13 equilibrium points are present are depicted in Fig. 6. We see that for $A = -0.1556$, that is just below the second critical level A_2, the configuration space (x, y) is dominated by the BOC corresponding to the points of equilibrium L_{14} and L_{15}, which appear in this interval. However as we further reduce the value of the oblateness these area of these BOC
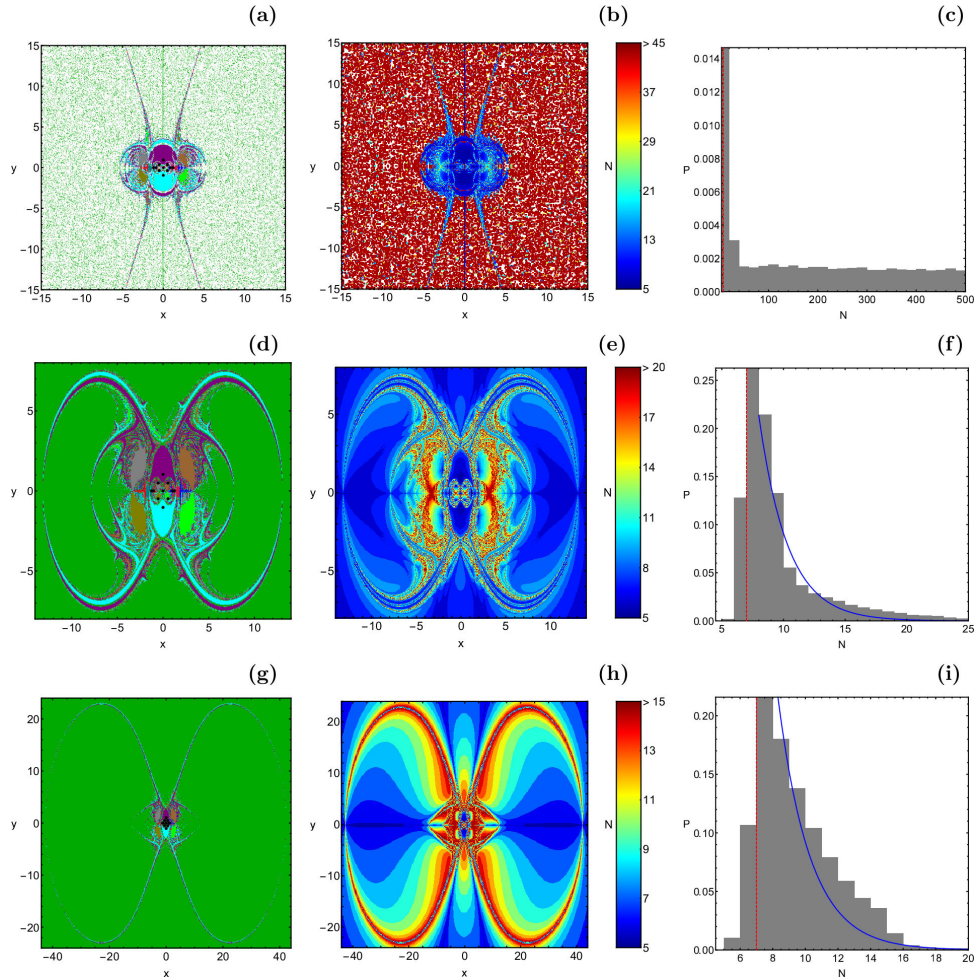
Figure 5. (First column): Color-coded plots showing the NR BOC on the configuration space (x, y), when 11 equilibrium points exist. The colors denoting the 11 numerical attractors (libration points) are the same as in Fig. 4. (Second column): Distributions of the corresponding required numbers of iterations. (Third column): Histograms with the corresponding probability distributions. (First row): $A = -0.08718$; (Second row): $A = -0.15$; (Third row): $A = -0.1555$. (Color figure online).

is considerably confined.

For $A = -0.2706$, which is a level close to the critical level A_3, it is observed in panel (g) of Fig. 6 that the BOC corresponding to the libration points L_8, L_9, L_{12}, and $L_1 3$ have almost disappeared, while at the same time the BOC of the points of equilibrium L_7 and L_{10} have been highly suppressed. These facts indicate that the dynamical properties of the Hamiltonian system are about to change by the mutual annihilation of the equilibrium points L_8, L_9, L_{12}.

4.4. Case IV: 9 equilibrium points

In Fig. 7 we present the BOC on the configuration space (x, y) for the fourth interval (A_4, A_3), when 9 equilibrium points exist. In this case, the overall geometrical shape
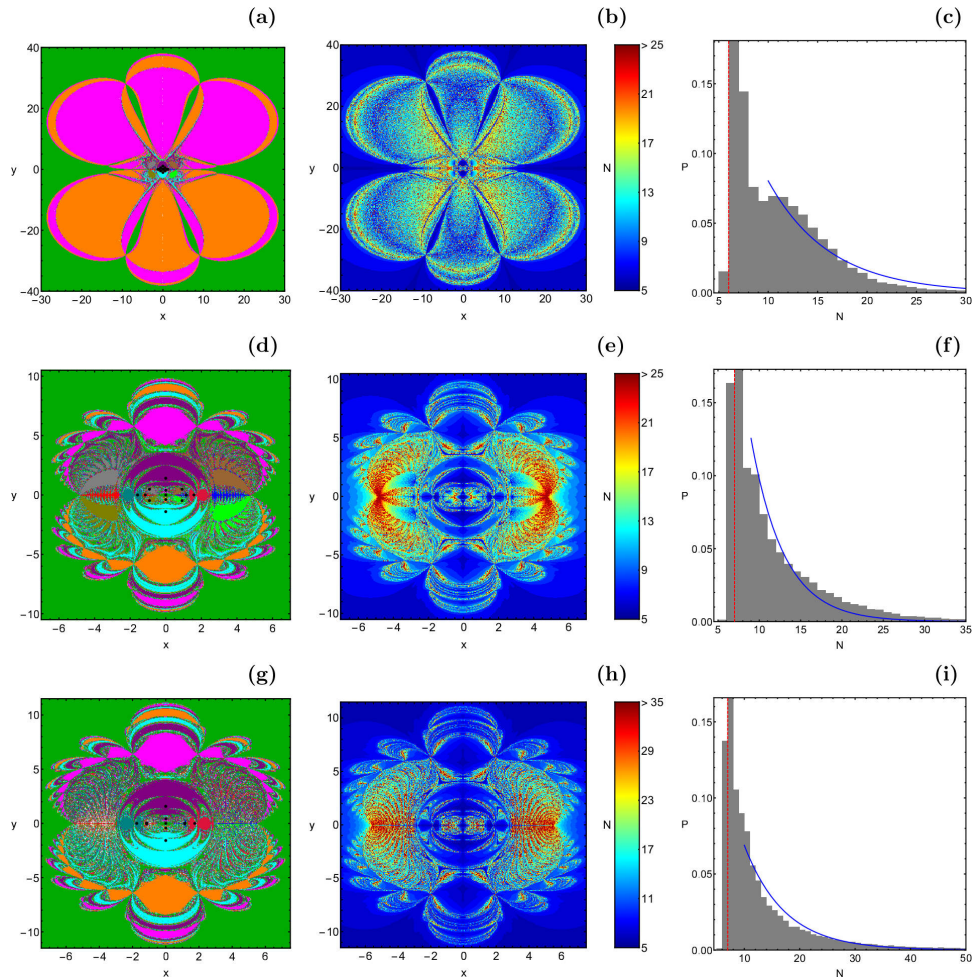
Figure 6. (First column): Color-coded plots showing the NR BOC on the configuration space (x, y), when 13 equilibrium points exist. The colors denoting the 13 numerical attractors (libration points) are the same as in Fig. 4, with the following addition to the palette: L_{14} (magenta); L_{15} (orange). (Second column): Distributions of the corresponding required numbers of iterations. (Third column): Histograms with the corresponding probability distributions. (First row): $A = -0.1556$; (Second row): $A = -0.25$; (Third row): $A = -0.2706$. (Color figure online).

of the BOC is not highly affected by the decrease on the oblateness parameter. Nevertheless, the parameter A mostly affects the size of the BOC. In other words, even though the overall shape remains almost the same, its size on the physical plane (x, y) grows drastically. Moreover, also the distributions of the iterations remain the same, with decreasing value of the oblateness.

4.5. Case V: 5 equilibrium points

The results of the last case are given in Fig. 8. Now the dynamical system has only five equilibrium points, that is the same total number as in the case of the classical RTBP. In the second row of Fig. 8, where $A = -0.5$, one can observe the
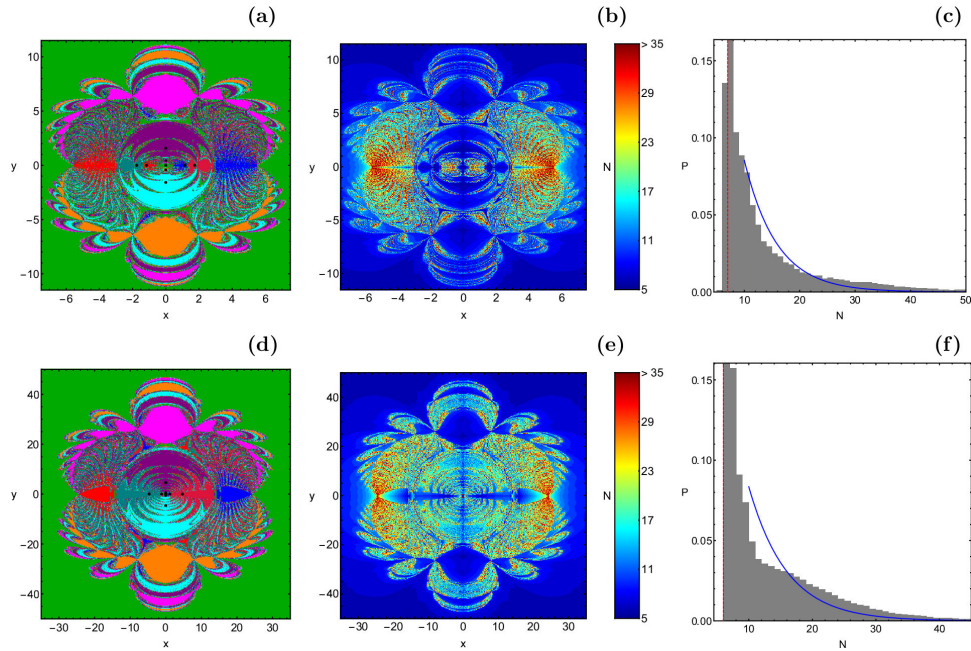
Figure 7. (First column): Color-coded plots showing the NR BOC on the configuration space (x, y), when 9 equilibrium points exist. The colors denoting the 9 numerical attractors (libration points) are the same as in Fig. 4. (Second column): Distributions of the corresponding required numbers of iterations. (Third column): Histograms with the corresponding probability distributions. (First row): $A = -0.2707$; (Second row): $A = -0.33$. (Color figure online).

presence of two main regions which are composed of initial conditions for which the NR displays non-convergence. Additional numerical calculations reveal that these starting conditions are true non-converging points which do not show any signs of convergence to one of the numerical attractors (equilibrium points), even after 1000 iterations. More information about the non-converging points of the RTBP system with prolate primaries will be given in the next Section.

With decreasing value of the oblateness we see that the area of the BOC shrinks and they are confined near the origin. For example, when $A = -1$ (see third row of Fig. 8), for each of the four libration points L_7, $L_{1}0$, L_{14}, and L_{15} we have only one main BOC, while the area of the BOC corresponding to the central point of equilibrium L_1 extends to infinity, as usual. Another interesting fact which occur when the value of A decreases is that the required time of iterations is also reduced, according to the second and third column of Fig. 8.

5. Influence of the oblateness A

To determine in detail the dependence of the convergence properties of the system on the oblateness parameter A, we classified 1000 grids of 1024×1024 initial conditions (x_0, y_0), with $-10 \leq x \leq +10$, and $-10 \leq y \leq +10$, for the range $A \in [-1, 0)$.

Panel (a) of Fig. 9 shows the average required number of iterations $< N >$, as a function of the oblateness A. It is seen, that $< N >$ displays local maxima (peaks) at the critical levels of the parameter A. Our numerical computations suggest that for
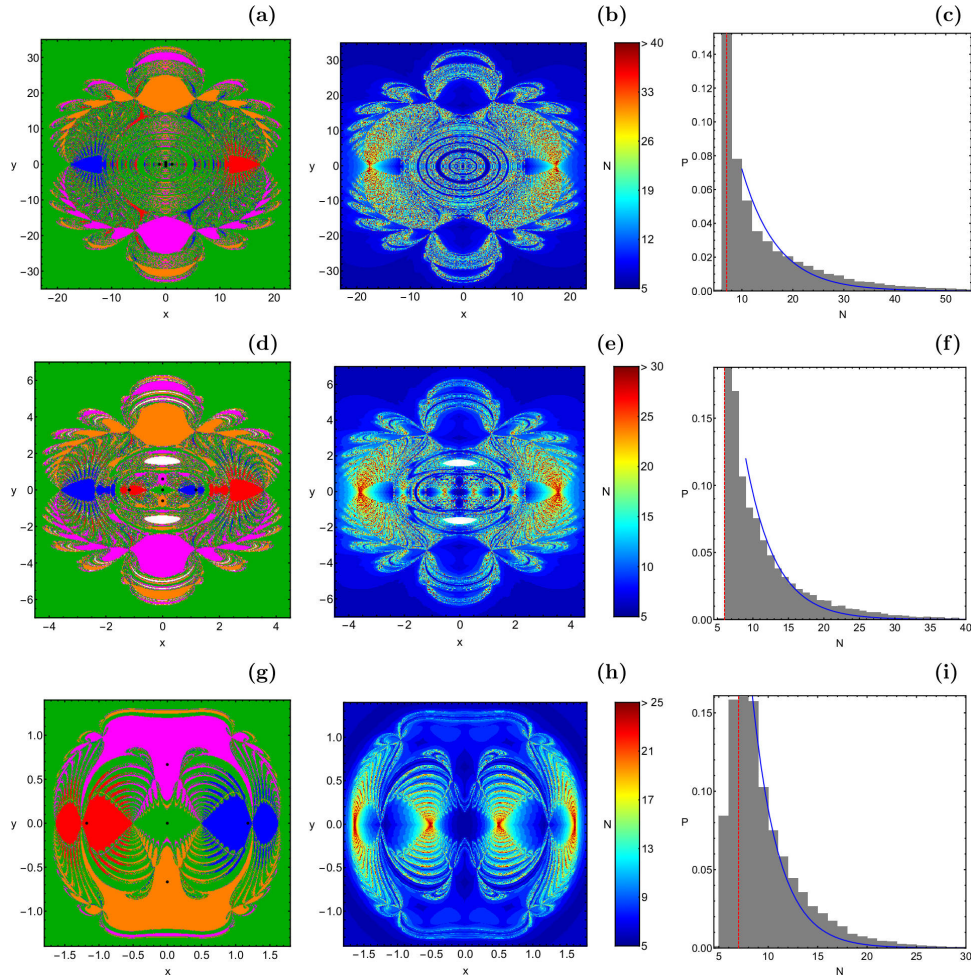
Figure 8. (First column): Color-coded plots showing the NR BOC on the configuration space (x, y), when only 5 equilibrium points exist. The colors denoting the 5 numerical attractors (libration points) are the same as in Fig. 4. (Second column): Distributions of the corresponding required numbers of iterations. (Third column): Histograms with the corresponding probability distributions. (First row): $A = -0.34$; (Second row): $A = -0.5$; (Third row): $A = -1$. (Color figure online).

$A < -0.55$ the average value of required iterations remains completely unperturbed at $< N >= 5$.

The histograms shown in Figs. 4-8 can be used for extracting additional results, regarding the convergence properties of the NR method. For instance, we can use the Laplace distribution for obtaining the best fits of the tails of the histograms (see blue solid lines in the histograms). We choose to use the Laplace distribution because this is the most natural choice, particularly in systems where we encounter transient chaos (see e.g., [21–23]).

The Laplace probability density function (PDF) is given by

$$P(N|l, d) = \frac{1}{2d} \begin{cases} \exp\left(-\frac{l-N}{d}\right), & \text{if } N < l \\ \exp\left(-\frac{N-l}{d}\right), & \text{if } N \geq l \end{cases}, \tag{5.1}$$

(a)

(b)

(c)

(d)
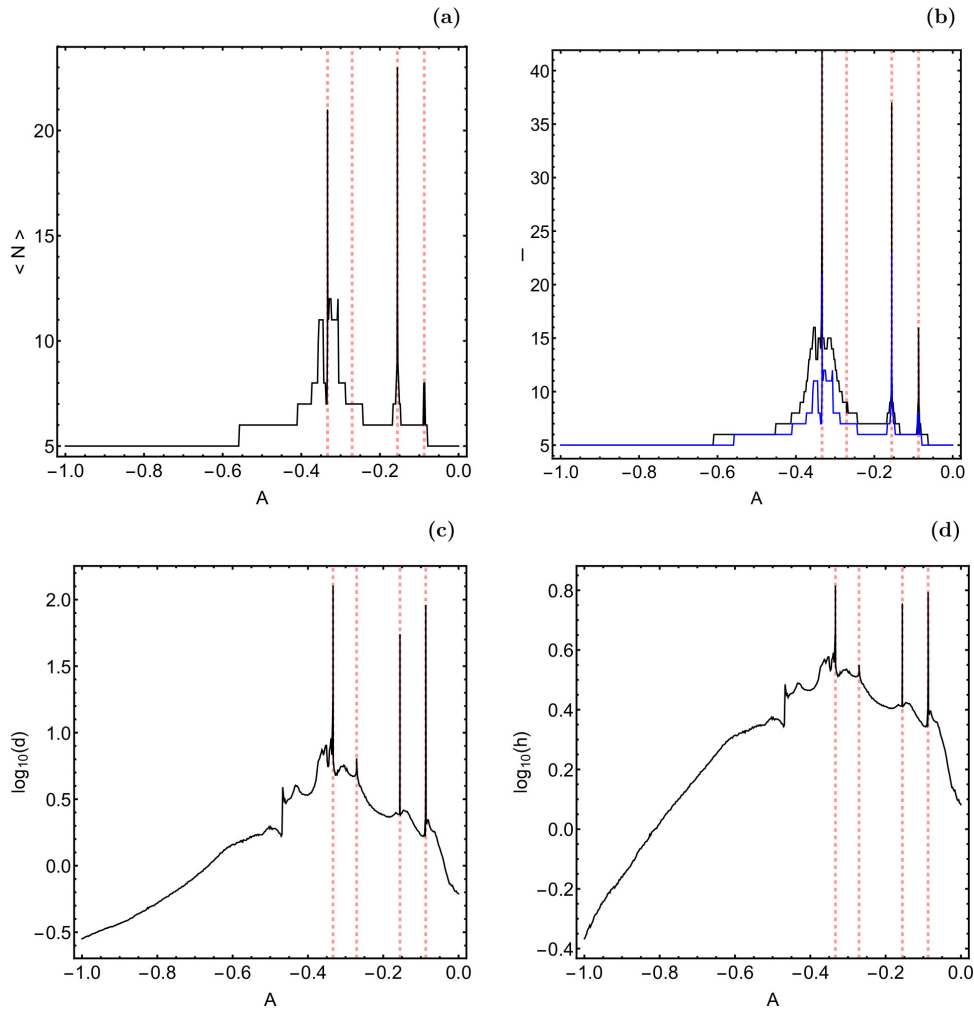
Figure 9. Parametric evolution of the (a-upper left): most average number of iterations $< N >$; (b-upper right): location parameter l; (c- lower left): diversity d; (d-lower right): differential entropy h, as a function of the oblateness A. With blue color in panel (b) we denote the parametric evolution of $< N >$. The red, dashed, vertical lines indicate the four critical values of the oblateness. (Color figure online).

where the parameters l and $d > 0$ are the location parameter and the diversity, respectively. From the PDF we need only the $N \geq l$ part because the Laplace distributions refer only to the tails of the probability histograms.

In panels (b) and (c) of Fig. 9 we present the parametric evolution of the location parameter l and the diversity d, respectively, as a function of A. In part (b) we also included, for comparison reasons, using blue color, the evolution of the $< N >$ of the iterations. One can observe that in general terms l is relatively close to the average number of required iterations (almost always $|l- < N >| \leq 2$). This implies that the Laplace probability density function (PDF) can satisfactorily fit the tails of the probability histograms. According to the diagram shown in part (c) of Fig. 9 the diversity is, in most of the cases, low ($d < 3$), thus indicating the dispersion
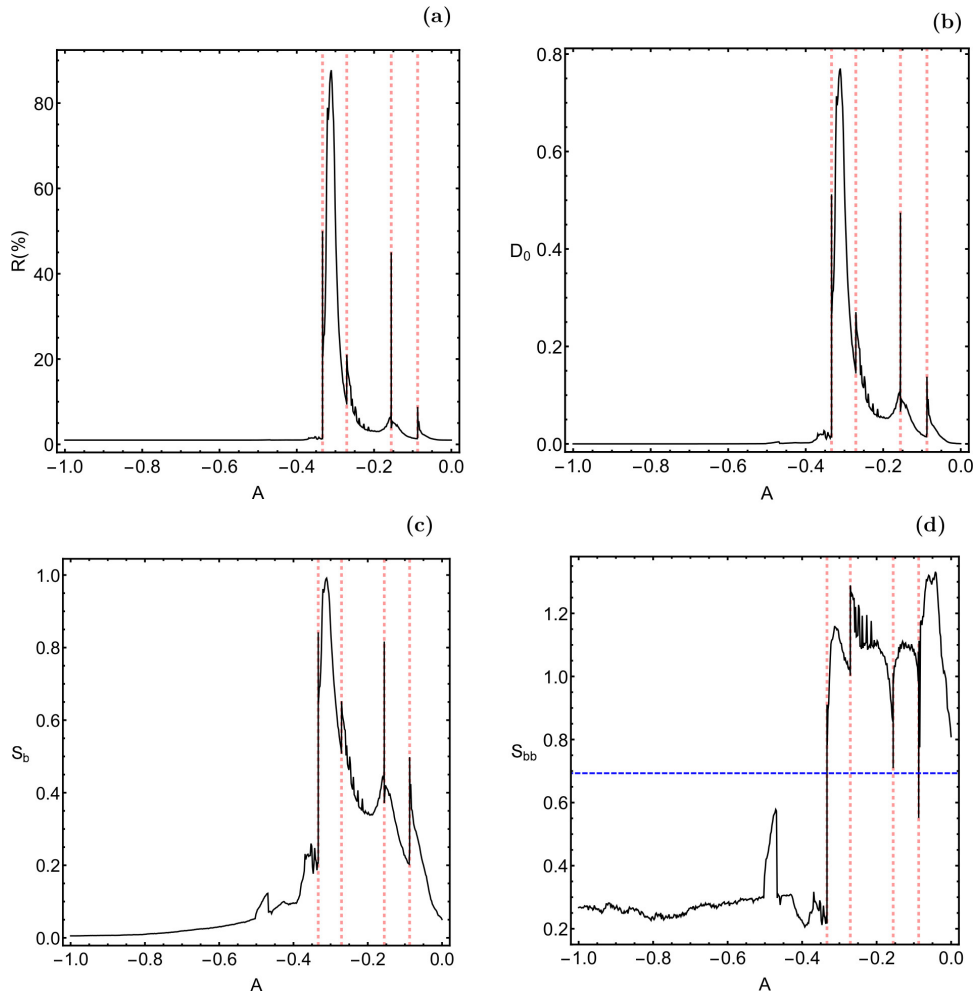
Figure 10. Parametric evolution of the (a-upper left): area on the configuration space (x, y) corresponding to a fractal-like geometry, (b-upper right): uncertainty or fractal dimension D_0, (c-lower left): basin entropy S_b and (d-lower right): boundary basin entropy S_{bb}, as a function of the oblateness A. The red, dashed, vertical lines indicate the four critical values of the oblateness. The blue, dashed, horizontal line denotes the critical value $\log 2$. (Color figure online).

of the values of N is very close to $< N >$. On the other hand, in the vicinity of the critical values of the oblateness the diversity exhibits a local maximum (peaks). Panel (d) of Fig. 9 illustrates the parametric evolution of the differential entropy $h = 1 + \ln(2d)$, where d is the diversity. One can see, that the evolution of both d and h displays similar overall patterns.

In the previous section we seen in the BOC presented in Figs. 4-8 that in many studied cases the basin boundaries seem very fractal. In panel (a) of Fig. 10 we present the evolution of the area on the configuration space ($R\%$) covered by regions with fractal-like geometry, as a function of the parameter A. One of the most convenient ways of measuring the degree of fractality of a system is by computing the uncertainty or fractal dimension D_0 (see e.g., [24]), thus following the computational
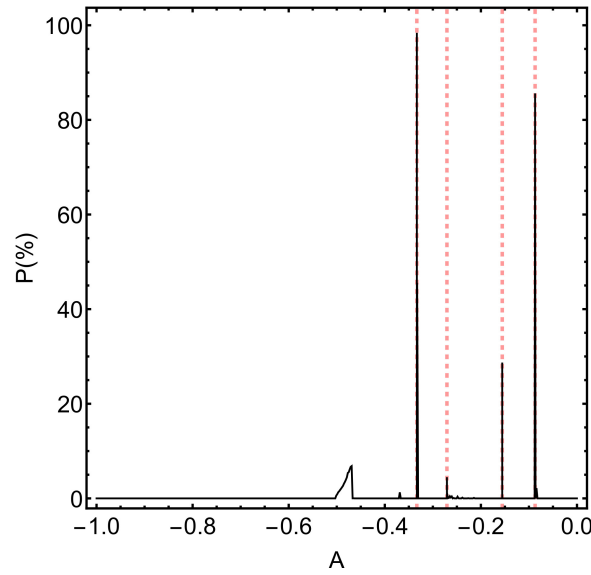
Figure 11. Parametric evolution of the area on the (x, y) plane corresponding to non-converging initial conditions, as a function of the oblateness A. The red, dashed, vertical lines indicate the four critical values of the oblateness. (Color figure online).
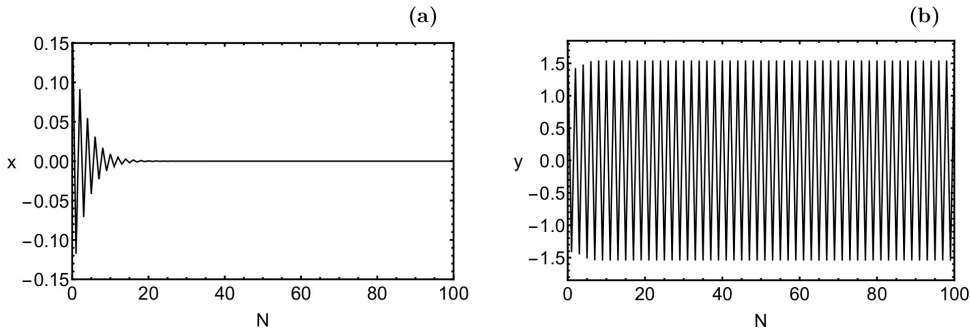
Figure 12. Parametric evolution of the (a-left): x coordinate and (b-right): y coordinate, as a function of the number N of iterations of a characteristic non-converging initial condition with: $x_0 = -0.2$ and $y_0 = 1.8$, while $A = -0.5$.

methodology used in [25, 26]. At this point, we would like to emphasize that the degree of fractality is an intrinsic property of the system and therefore it does not depend on the particular initial conditions we use for its calculation. Fig. 10(b) shows the evolution of the uncertainty dimension, as a function of the oblateness A. Near the critical level A_4 the fractal dimension tends to 1, which implies zero fractality. Moreover, in the vicinity of all critical levels of the oblateness the fractal dimension exhibits local maxima (peaks).

Another efficient way for quantitatively measuring the degree of fractality of a system is by computing the so-called basin entropy [27,28]. This method determines the fractality of a basin diagram by the process of examination of its topological properties. The parametric evolution of the basin entropy S_b, as a function of the oblateness A, is illustrated in panel (c) of Fig. 10. Once more, we note that in the

vicinity of all the critical values of A there are four local maxima of S_b. Taking into account the outcomes of panels (a)-(c) of Fig. 10, we may argue that three different methods (i.e., the area of the fractal-like regions, the fractal dimension along with the basin entropy) suggest that the degree of the fractality of the BOC on the configuration space (x, y) is high near the critical levels of A. At this point, we would like to emphasize that the particular evolution of the three quantities (i.e., the area of the fractal-like regions, the uncertainty dimension and the basin entropy) is very similar, which is an extraordinary numerical finding.

Apart from the basin entropy there is also the boundary basin entropy S_{bb} [27], from which we can extract additional information about the fractal geometry of the BOC. The parametric evolution of S_{bb} is given in panel (d) of Fig. 10. From this type of plot we can also deduce information regarding the degree of fractality of the BOC on the configuration space. More specifically, we can use the so-called "log 2 criterion", according to which if $S_{bb} > \log 2$ then the basin boundaries are certainly fractal (here note that the converse statement is not valid). As it is seen in panel (d) of Fig. 10 the basin boundaries are certainly fractal when $A > A_4$. Once more, the lowest values of S_{bb} are reported in the fourth interval, that is when $A < A_4$, where only five numerical attractors exist.

At this point, we would like to briefly discuss the efficiency of the NR method. The classification of the 1000 grids of initial conditions suggested that there are cases at which non-converging points exist. In Fig. 11 we provide the parametric evolution of the area on the configuration space (x, y) covered by non-converging initial conditions, as a function of the oblateness A. We see that the non-converging points emerge mainly in the vicinity of the critical values of A, where the dynamics of the system changes. In particular, for $A = A_1$ and $A = A_4$ more than 80% of the physical plane is occupied by non-converging initial conditions. In the same plot, one can observe an additional small peat around $A = 0.47$, where non-converging points also exist.

For the RTBP system with prolate primaries the multivariate Newton-Raphson scheme reported only non-converging initial conditions, for some values of the oblateness. Our computations indicate that for these starting points the iterative method fluctuates between real numbers, without displaying any numerical evidence of convergence. Additional calculations revealed that the same behavior is still valid even after extremely large number of iterations $N = 10^4$. In panels (a-b) of Fig. 12 we present the evolution of the x and y coordinates, respectively, as a function of the number N of iterations of a characteristic non-converging initial condition. For the x coordinate the NR method quickly converges to zero after about 15 iterations, while for the y coordinate is always fluctuates between two opposite numbers, thus resulting to a non-converging initial condition.

6. Discussion

The present article is in fact a continuation of [17]. The scope of the article was a numerical investigation of the convergence properties of the RTBP with prolate primaries. By integrating large sets of initial conditions we obtained the NR BOC, by means of color-coded basin diagrams. Moreover, we explored how the oblateness parameter A influences the convergence properties of the Hamiltonian system. To determine the level of fractality in the dynamics we calculated the fractal dimension, along with the (boundary) basin entropy.

In this work we demonstrated for the first time how the oblateness of the RTBP with prolate primaries influences the overall properties of the system. Additionally, we relate also for the first time different techniques for measuring how fractal a dynamical system is. More specifically, we computed and compared the results of the uncertainty (fractal) dimension and the (boundary) basin entropy. On this basis, we claim that all the presented results of the article are novel and interesting, while they contribute to our existing knowledge on the convergence properties of Hamiltonian systems.

The numerical routine of the Newton-Raphson iterative method was written in standard `FORTRAN 77` [29]. For the classification of the starting points on the configuration space, we needed roughly about 2.5 minutes of CPU time, per grid, using a Quad-Core i7 vPro 4.0 GHz processor. The version 11.3 of Mathematica® [30] has been deployed for constructing all the graphics of the paper.

References

[1] V. Szebehely, *Theory of Orbits*, Academic Press, New York, 1967.

[2] J. K. Beatty, C. C. Petersen and A. Chaikin, *The New Solar System*, 4th ed., Cambridge University Press, Cambridge, 1999.

[3] R. K. Sharma and P.V. Subba Rao, *Collinear equilibria and their characteristic exponents in the restricted three-body problem when the primaries are oblate spheroids*, Celestial Mechanics, 1975, 12, 189-201.

[4] A. S. Safiya Beevi and R. K. Sharma, *Oblateness Effect of Saturn on Periodic Orbits in the Saturn-Titan Restricted Three-Body Problem*, Astrophysics and Space Science, 2012, 340, 245-261.

[5] V. S. Kalantonis, V. V. Markellos and E. A. Perdios, *Computing periodic orbits of the three-body problem: Effective convergence of Newton's method on the surface of section*, Astrophysics and Space Science, 2005, 298, 441-451.

[6] V. S. Kalantonis, C. N. Douskos and E. A. Perdios, *Numerical Determination of Homoclinic and Heteroclinic Orbits at Collinear Equilibria in the Restricted Three-Body Problem with Oblateness*, Celestial Mechanics and Dynamical Astronomy, 2006, 94, 135-153.

[7] V. S. Kalantonis, E. A. Perdios and A. E. Perdiou, *The Sitnikov family and the associated families of 3D periodic orbits in the photogravitational RTBP with oblateness*, Astrophysics and Space Science, 2008, 315, 323-334.

[8] V. V. Markellos, K. E. Papadakis and E. A. Perdios, *Non-Linear Stability Zones around Triangular Equilibria in the Plane Circular Restricted Three-Body Problem with Oblateness*, Astrophysics and Space Science, 1996, 245, 157-164.

[9] V. V. Markellos, A. E. Roy, M. J. Velgakis and S. S. Kanavos, *A Photogravitational Hill Problem and Radiation Effects on Hill Stability of Orbits*, Astrophysics and Space Science, 2000, 271, 293-301.

[10] R. K. Sharma, *The periodic orbits of the second kind in terms of Giacaglia's variables with oblateness*, Earth Moon Planets, 1989, 45, 213-218.

[11] R. K. Sharma, *Periodic orbits of the third kind in the restricted three-body problem with oblateness*, Astrophysics and Space Science, 1990, 166, 211-218.

[12] J. Singh and O. Leke, *Equilibrium points and stability in the restricted three-body problem with oblateness and variable masses*, Astrophysics and Space Science, 2012, 340, 27-41.

[13] J. Singh and O. Leke, *Effect of oblateness, perturbations, radiation and varying masses on the stability of equilibrium points in the restricted three-body problem*, Astrophysics and Space Science, 2013, 344, 51-61.

[14] E. E. Zotos, *How does the oblateness coefficient influence the nature of orbits in the restricted three-body problem?*, Astrophysics and Space Science, 2015, 358, 10.

[15] E. E. Zotos, *On the NewtonRaphson basins of convergence of the out-of-plane equilibrium points in the Copenhagen problem with oblate primaries*, International Journal of Non-Linear Mechanics, 2018, 103, 93-103.

[16] A. E. Perdiou, E. A. Perdios and V. S. Kalantonis, *Periodic orbits of the Hill problem with radiation and oblateness*, Astrophysics and Space Science, 2012, 342, 19.

[17] E. E. Zotos, *Fractal basins of attraction in the planar circular restricted three-body problem with oblateness and radiation pressure*, Astrophysics and Space Science, 2016, 361, 181.

[18] E. E. Zotos, *Basins of convergence of equilibrium points in the pseudo-Newtonian planar circular restricted three-body problem*, Astrophysics and Space Science, 2017, 362, 195.

[19] J. Nagler, *Crash test for the Copenhagen problem*, Physical Review E, 2004, 69, 066218.

[20] J. Nagler, *Crash test for the restricted three-body problem*, Physical Review E, 2005, 71, 026227.

[21] A. E. Motter and Y. C. Lai, *Dissipative chaotic scattering*, Physical Review E, 2001, 65, 015205.

[22] J. M. Seoane, J. Aguirre, M. A. F. Sanjuán and Y. C. Lai, *Basin topology in dissipative chaotic scattering*, Chaos, 2006, 16, 023101.

[23] J. M. Seoane and M. A. F. Sanjuán, *Exponential decay and scaling laws in noisy chaotic scattering*, Physics Letters A, 2008, 372, 110-116.

[24] E. Ott, *Chaos in Dynamical Systems*, Cambridge University Press, Cambridge, 1993.

[25] J. Aguirre, J. C. Vallejo and M. A. F. Sanjuán, *Wada basins and chaotic invariant sets in the Hénon-Heiles system*, Physical Review E, 2001, 64, 066208.

[26] J. Aguirre, R. L. Viana and M. A. F. Sanjuán, *Fractal structures in nonlinear dynamics*, Reviews of Modern Physics, 2009, 81, 333-386.

[27] A. Daza, A. Wagemakers, B. Georgeot, D. Guéry-Odelin and M. A. F. Sanjuán, *Basin entropy: a new tool to analyze uncertainty in dynamical systems*, Scientific Reports, 2016, 6, 31416.

[28] A. Daza, A. Wagemakers, B. Georgeot, D. Guéry-Odelin and M. A. F. Sanjuán, *Basin Entropy, a Measure of Final State Unpredictability and Its Application to the Chaotic Scattering of Cold Atoms.*, M. Edelman et al. (eds.), Chaotic, Fractional, and Complex Dynamics: New Insights and Perspectives, Understanding Complex Systems, Springer International Publishing AG, 2018.

[29] H. P. Press, S. A. Teukolsky, W. T. Vetterling and B. P. Flannery, *Numerical Recipes in FORTRAN 77*, 2nd Ed. Cambridge University Press, Cambridge, 1992.

[30] S. Wolfram, *The Mathematica Book*, Fifth Edition, Wolfram Media, Champaign, 2003.